Low-concentration detection of H_2S using temperature-dependent Cr-doped cobalt-oxide gas sensors

V. Manikandan [a,*], G. Ayyannan [b], Rajaram S. Mane [c], Iulian Petrila [d], Manickam Selvaraj [e,f], Robert D. Crapnell [g], Craig E. Banks [g]

[a] *Department of Physics, SRMV College of Arts and Science, Coimbatore 641020, India*
[b] *Department of Chemistry, SRMV College of Arts and Science, Coimbatore 641020, India*
[c] *Center for Nanomaterial & Energy Devices, SRTM University, Nanded 431606, India*
[d] *Faculty of Automatic Control and Computer Engineering, Gheorghe Asachi Technical University of Iasi, Iasi 700050, Romania*
[e] *Department of Chemistry, Faculty of Science, King Khalid University, Abha 61413, Saudi Arabia*
[f] *Research Centre for Advanced Materials Science, King Khalid University, Abha 61413, Saudi Arabia*
[g] *Faculty of Science and Engineering, Manchester Metropolitan University, M1 5GD, UK*

A B S T R A C T

Among the existing metal-oxide gas sensors, cobalt oxide has the flexibility to revise the morphology through Cr-dopant to enhance sensing properties. Sensitive-surface of the chromium-doped cobalt oxide has proven its effective sensing nature to hydrogen sulfide gas. Interestingly, chromium-dopant increases the surface area, leading to particle size reduce and produces the more active sites for gas molecules. Also, the dopant creates impurity phases on the material which extends the sites for more reaction. To confirms these characteristics, the photoluminescence spectra showed intense peak that mimics the faster transport of electron to accelerate the sensing reaction. According to sensing measurement, the doped sensor is showing three-fold increase of response to 10 ppm gas and also, it detects the 2 ppm efficiently. The doped sensor warrants the stable response to gas due to higher reproducibility. Notably, the doped sensor detects the 1 ppm of gas at 120 s and recovery itself around 200 s. The doped sensor imparts response at room-temperature, affirming sensitive-surface. The doped sensor has shown the capable under humidity environment through response.

1. Introduction

Growing population has increased the industries of petroleum refining, natural gas production, waste water management, coal mining and paper mills[1]. These industries produce the poisonous and flammable hydrogen sulphide and also, drainage water release the same gas [2]. It makes different health disorders in accordance to the concentration level [3]. On the other hand, hydrogen sulfide caused corrosion which harms metallic equipment [4]. A portion of fuel gases containing H_2S gas and it can oxidize to SO_2 which causes air pollution [5,6]. Hence, detection of the H_2S is crucial [7]. In past, there are number of research works regarding the development of various H_2S sensors which couldn't demonstrate sensing at room temperature ($\geq 35^{\circ}C$). Most of the reports revealed high-temperature sensing operations ($\geq 265^{\circ}C$) [8–12].

Selection of potential sensor materials is one of the critical issues in sensor technology. Among different metal oxides, the cobalt oxide is formed as two-component system (CoO and Co_3O_4). The two-component system enriches the adsorption sites for gas sensing. Cobalt oxide (Co_3O_4) is easily fortified for room-temperature sensing applications through doping [13–15]. Basically, it has hexagonal closed packed, face-centred cubic and epsilon crystal structures [16]. In oxide form, cobalt carries different spin states such as high, low and intermediate for obtaining better optical properties which can be used for gas sensors, solar cells, energy storage devices, field effect transistors, anode materials in batteries and photocatalyst etc [17–19]. The applications of cobalt oxide are closely related to its particle size. Nowadays, the experimental production of the cobalt oxide has increased due to its high adsorption rate, considerable surface defects and fast diffusivity. Crystallite size of the cobalt oxide impacts their phase formation and oxidation/reduction reaction [20]. If the size of the nanoparticle is 20 nm, the redox activity of cobalt-based nanoparticle is uncertain which can be piloted by fast kinetics, small-size, oxide support and uniform

distribution of nanoparticles [21,22]. It ample the electron migration during sensor detection which turns more reliable for sensors application [23]. Long-term thermal stability, good conductivity and better mechanical strength have enables to use as an energy-related device [24, 25].

As above-mentioned properties are warranting the good sensing nature. Here, the material suitability is determined by the active sites and electrical conductivity. The access of active sites is reduced by low electrical conductivity which adversely reflect on the performance of envisaged sensor material [26]. Hence, different approaches such as doping, control the growth of metal phase, incorporation of vacancies and conductive support are being utilized to enhance the electrical conductivity [27–29]. These approaches have been enriched through nano-structuring process which affords a huge reactive site with large specific surface area. Also, lowering electronic energy promotes the high conductivity [30–34]. Even though, a wide range of research activities is performed in this area, it is still difficult to create cobalt oxide-based materials with better electrical nature. Here, the doping approach is used to examine the cobalt oxide -based nanomaterials for H_2S gas sensing application.

Chromium oxide is high temperature resistant material which assures the low-operating temperature for gas sensor application [35]. It has shown ability to control particle size and producing small-size particles with high activation energy. Also, it has high reproducibility, low-response to water vapor and high response to target gas, suggesting moderate stability [36]. Chromium oxide is a selective material as compared to other metal oxides because it reacts into two different ways such as lattice oxygen and interacting through surface state [37]. This means that the reaction time of chemisorption at the surface is significantly less than the time it takes for adsorbed species to diffuse into bulk. The use of a binder is not necessary because the chromium oxide particles cling tightly to another particle and substrate [38]. Chromium oxide also endows low resistivity, antiferromagnetic and good optical nature which is added advantages for sensor. Moreover, the chromium can be easily doped into the cobalt lattice, maintaining host matrix phase [39]. The chromium oxide properties listed above may support the substantial sensing results.

Here, the sensor material is synthesized by simple and effective chemical co-precipitation method. The particle size is reduced due to the doping. Through doping, the morphology of the material is greatly revised. In this work, the Cr-doped sensor outperformed the undoped sensor. The doped sensor performs well in both platform of room and higher temperature. The sensor senses the minimum and maximum of H_2S gas (1–100 ppm). The sensor response is enhanced by Cr doping. Also, the doped sensor has quickly detected the H_2S gas. The objective of the work is to reduce the operating temperature and flexible the surface through dopant. These helps to change surface area and influence the sensing reaction greatly. In addition to these, charge transfer and defects states are achieved.

2. Experimental details

2.1. Chemicals

The source materials of cobalt(II) nitrate hexahydrate ($Co(NO_3)_2{\cdot}6H_2O$) and chromium(III) nitrate nonahydrate ($Cr(NO_3)_3{\cdot}9H_2O$) were purchased from Sigma-Aldrich. The sodium hydroxide pellets (NaoH) is obtained from Nice Chemicals Limited. The glass items are procured from Borosil company.

2.2. Synthesis of Co_3O_4 and Cr-doped Co_3O_4 nanoparticles

The cobalt nitrate and chromium nitrate nonahydrate were dissolved into separate 100 mL water contained beaker according to stoichiometry ($Cr_xCo_{3-x}O_4 : x = 0.0, 0.2, 0.4$). These materials are stirred well using magnetic stirrer. The solution of chromium is poured to the cobalt solution and stirrer again till to obtain homogeneous solution. The precipitate agent of sodium hydroxide solution was added (dropwise) solution until to reach pH 11. The precipitate is washed with Milli-Q water to eliminating sodium hydroxide and unreacted impurities. Later, the precipitate is dried through microwaves, and it grounded manually (mortar-pestle). Finally, the product was annealed at 400 ℃ for 4 h to get rid of organic contaminants.

2.3. Characterizations

Crystallographic reflection planes of prepared nanomaterial is obtained from the X-ray diffraction patterns (D8 Advanced Eco Bruker Germany). Surface appearances is confirmed through field-emission scanning electron microscopy (ZEISS GeminiSEM 500 Acceleration voltage 0.02 – 30 kV) and transmission electron microscopy (Technai G^2 30 operated at 200 kV) digital images. Outward chemical composition, oxidation states and surface functionalization were analyzed through X-ray photoelectron spectroscopy (XPS, AXIS Supra$^+$). Absorption band edges are located through UV absorbance measurements (Jasco UV V-770). Structural defects are studied from luminescence spectrums (FP-8300). Raman spectroscopy was used to analyze the phase purity of Co_3O_4 and Cr-doped Co_3O_4 nanoparticles (Laser Raman Invia II). Surface area measurement is done through BET (BELSORP-maxII-Constant volume gas adsorption method + AFSM). Gas sensing measurement is carried out with custom-made chamber. The gas sensor testing device was composed of gas chamber which was computerized controlled for measuring temperature and gas concentration. The signal of the sensors are collected by computerized data acquisition system; a computerized upgrade version of Figaro gas sensor test chamber. The ratio of the sensor resistance in an air flow (R_a) to its steady-state resistance in an analyte gas flow (R_g) is referred to as the gas response. The response is measured at 20 — 5 0 0 ° C by switching between the mixture of gas and dry air. Sensing setup is shown in Fig. S1.

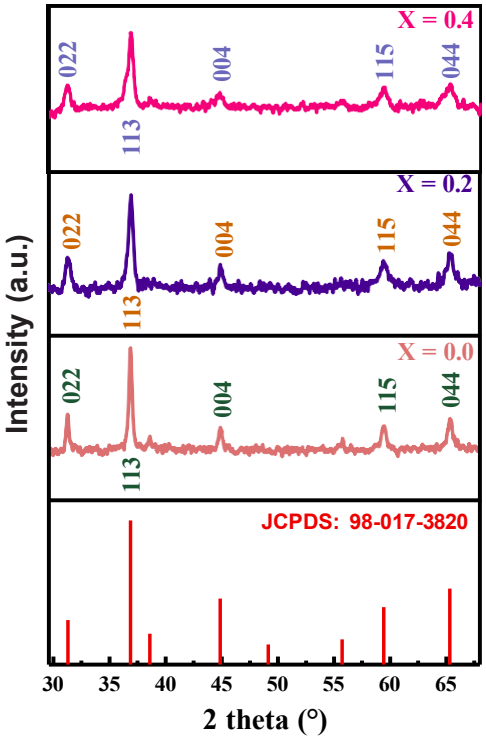

Fig. 1. The XRD patterns of $Cr_xCo_{3-x}O_4 : x = 0.0, 0.2, 0.4$ nanoparticles.

3. Results and discussion

The XRD patterns of the Co_3O_4 and Cr-doped Co_3O_4 nanoparticles are displayed in Fig. 1 wherein, the formation of cubic crystal structure is confirmed. The cubic phase is retained after the substitution of Cr into a cobalt lattice. The (022), (113), (004), (115) and (044) reflection planes of XRD are ideally matched to the cubic Co_3O_4 phase (JCPDS card no: 98–017–3820), corroborating the growth of expected product. It is noted that all reflection planes are consistent. This suggests that cubic symmetry of cobalt lattice has not been altered during the substitution of chromium[40]. A systematic peak shift is not noticed at initial substitution of chromium. The (022) and (113) reflection planes attain higher angle shift and rest of the reflection planes shift to lower angle. This infers that some chromium ions occupy interstitial positions which is responsible for higher angle shift. Rest of the chromium replaces cobalt, indicates lower angle shift. The reflection planes follow the systematic shift mimicking the lower angle shift due to the increase of Cr substitution. Besides, the change of *d-spacing* values confirms the lower angle shift. Also, the lattice constant is varied from 8.069 to 8.075 Å which affirms the d-spacing change. Owing to the chromium substitution, the width of the peaks is broadened and intensity of the peaks decreased, suggesting decrease of crystallite size[41]. The crystallite size is calculated using Scherrer formula and it shows decrease of crystallite size from 34 nm for Co_3O_4 and 23–18 nm for Cr-doped Co_3O_4. The expansion of surface area is associated with gradual decrease of crystallite size[42].

Fig. 2(a-c) demonstrates the effect of Cr doping on the surface morphology of Co_3O_4 nanoparticles. The microstructure of the Co_3O_4 nanoparticles have petal morphology. These petals avail smooth surfaces which is oriented in different directions and distributed non-uniformly. Moreover, the nanoparticles are linked to each other particles by forming necklace like architecture. On incorporating Cr into Co_3O_4, the petal morphology translates to the spherical. Furthermore, the size of the particles is also reduced. Fundamentally, the smaller spherical particle avail high surface area for enhancing the adsorption of gas molecules. On increasing the Cr concentration, the particle size is decreased further. Along with spherical nanoparticles, few nanoflakes are observed in the microstructure of Cr-doped Co_3O_4, suggesting the chromium impedes the growth of nanoparticles. Also, the chromium substitution increases the particle size distribution[43]. EDS of the all materials is displayed in Fig. S2.

Fig. 3a displays the petals shape of undoped Co_3O_4 crystallites. Due to doping of chromium, these petal particles endure the size and structure change, as shown in Fig. 3(b-c). With an increase in dopant concentration, the size of the Cr-doped cobalt is clearly decreased. There is no obvious change in crystal structure of Co_3O_4 on Cr doping as selected area electron diffraction do not show substantial difference in Fig. 3(d- f). After Cr doping, the bright dotted rings are intensely visible, sug- gesting the changes of crystallinity. Each ring corresponds to (022), (113), (004), (115) and (044) reflection planes of the Co_3O_4. The par- ticle size distribution measurements are shown in Fig.S3. The undoped and doped Co_3O_4 showed 14–20 nm average particle size. The change in particle size after doping is clearly noticed. The surface area of the nanomaterial is 4.54, 10.32 and 36.85 m^2/g which indicates the surface area increase (Fig. S4). The dopant chromium enhances the surface area for gas sensing reaction.

The XPS spectrums of undoped and doped sensors reveals presence of respective elements as shown in Fig. 4(a-c), confirming successful incorporation of Cr into Co_3O_4 lattice. The XPS spectra of O 1 s are fitted to M-O (527.62 eV), O-H (529.37 eV), H_2O (532.19 eV) and M-OH (527.59 eV). In the O 1 s spectra, the undoped cobalt oxide has higher M-O bond, absorbed OH groups and adsorbed H_2O on the surface[44, 45]. The peak of H_2O and OH is shifted to lower BE due to the strong shielding of surface electrons[46]. The higher M-O bond may be linked to the different oxidation state of Co^{2+} showing the possibilities to induces more O^- species[45]. Due to doping, the binding energies of the spotted peaks accomplish shift as outcome of decrease in the binding energy. Additionally, M-OH bond is present at the initial concentration of Cr doping which manifests the moderate d-electron occupancy of orbital[47]. On doping of Cr, the sequel of binding energy decrease is increased further, implying oxygen atoms are bind to the mixed oxidation state of cobalt and chromium[48]. The cobalt is fitted to Co $2p_{3/2}$ (777.64 eV), Co $2p_{1/2}$ (793.07 eV) and two satellite peaks[49]. The binding energies associated with these fitted peaks are reduced due to doping which is also confirmed from FWHM of an individual peak. The dopant Cr is fitted to Cr $2p_{3/2}$ (582.38), Cr $2p_{1/2}$ (583.77), Cr^{3+}-OH (576.4 eV) and Cr^{3+}-OH (575.62 eV). Among these peaks, Cr^{3+}-OH and Cr^{3+}-O peaks indicate involvement of secondary chromium oxide (im- purity) on the surface of the host material[50]. The impurity is increased with dopant concentration. Such impurity enhances the surface charge density which can be endowed the better adsorption to gas molecules [51].

Fig. 5 depicts the Raman spectra of Co_3O_4 and Cr-doped Co_3O_4 nanoparticles. The undoped Co_3O_4 nanoparticles display vibration of 694.39 cm^{-1} for stretching mode, assuming the presence of moderate oxygen. In addition, low-intensity implies poor crystallinity. The position of 694 cm^{-1} peak is shifted to higher frequency and also, additional peak is observed along with intensity enhancement in the aspect of doping. In spectra, the peak appeared at 523.32 cm^{-1} has designated to Cr-vibrational mode[52]. Positive peak shift and higher intensity are corroborated. On further doping, the higher intensity peak of 696 cm^{-1} undergoes to negative shift, promising the higher oxygen defects[53]. Also, the low-intense peak of 487 cm^{-1} reveals the same negative shift but Cr-related peak shows the positive shift, suggesting increase of Cr content in Co_3O_4. In addition to this, the major peak at 694 cm^{-1} is directly connected to the lattice distortion. Usually, the peak at 694 cm^{-1} represents the active mode of sub-lattice and higher number valency cations present in the mode. Lattice distortion has originated from the above-mentioned sub-lattice shift[54]. According to Raman shift investigation, the obtained peaks are well related to the phase of Co_3O_4 [55].

Fig. 6(a-f) shows the absorbance spectra and Tauc's plot of undoped Co_3O_4 and Cr-doped Co_3O_4 nanoparticles. The undoped Co_3O_4 nanoparticles demonstrate the two absorption band edges around 476 and 712 nm [56]. The first band edge accords to visible region and later band edge conforms to near-infrared region. The observed visible and near-infrared region band edges are ascribed due to the charge transition

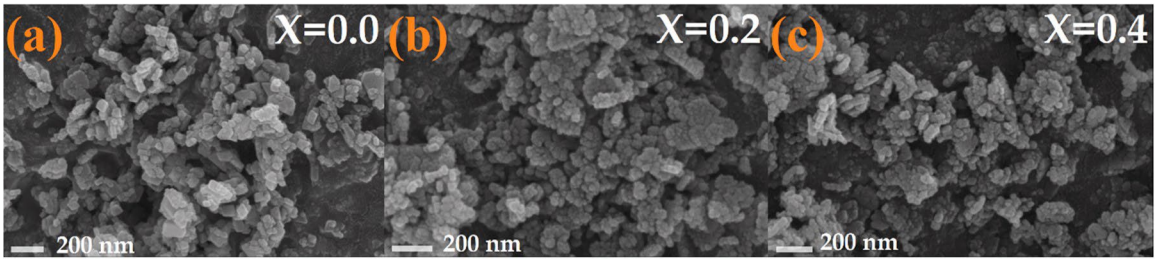

Fig. 2. (a-c) FE-SEM images of $Cr_xCo_{3-x}O_4$: $x = 0.0, 0.2, 0.4$ nanoparticles.

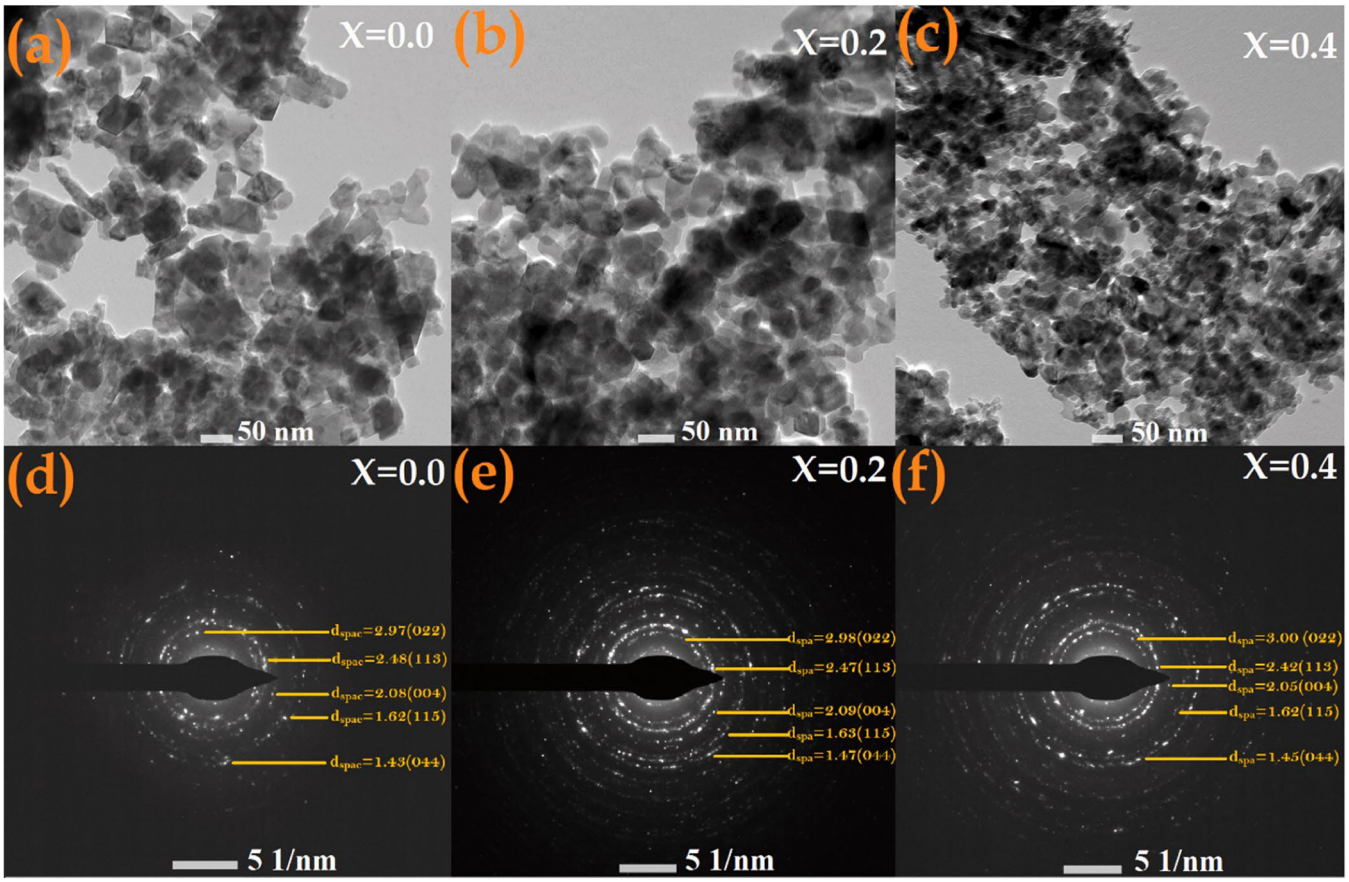

Fig. 3. TEM images of $Cr_xCo_{3-x}O_4$: x = 0.0, 0.2, 0.4 nanoparticles.: (a-c) microstructure, (d-f) SAED.

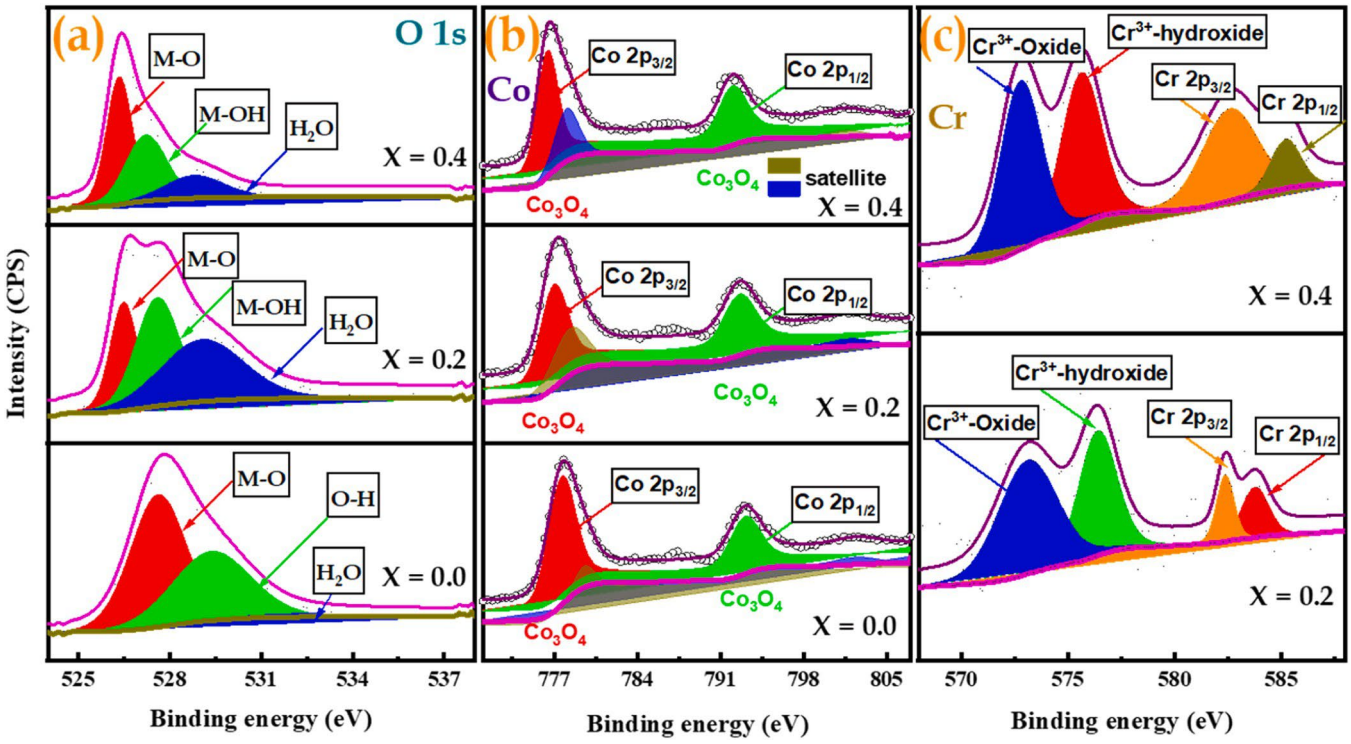

Fig. 4. XPS spectra of (a) O 1 s, (b) Co 2p and (c) Cr 2p of $Cr_xCo_{3-x}O_4$: x = 0.0, 0.2, 0.4 nanoparticles.

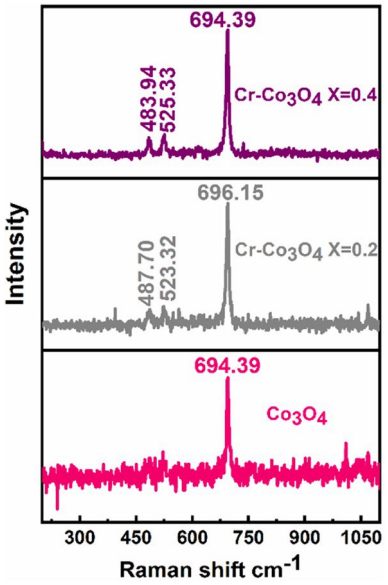

Fig. 5. Raman spectra of $Cr_xCo_{3-x}O_4$: $x = 0.0, 0.2, 0.4$ nanoparticles.

from O^{2-} to Co^{2+} and O^{2-} to Co^{3+} processes [57]. The two-band edge elevation in the material is caused by cobalt +2 oxidations (Co^{2+}) [41]. The Cr-doped Co_3O_4 nanoparticles disclose similar band edges but their wavelength attain shift. Therefore, the Cr dopant influences the absorbance properties of the Co_3O_4 nanoparticles. At low-level doping, the first band edge shifts to lower wavelength and second band edge shifts to higher wavelength. The obtained band edges are directly changing the band gap energy of the Co_3O_4. Similar type of shift is observed at higher concentration of chromium doping. The shorter and longer wavelength shift implies two band gap energies and its change. However, the electrons are localized and corresponding interaction to localized states results in change of the bandgap energy. The band edge to neared-infrared region is shifted to longer wavelength, suggesting red-shift. According to FE-SEM and TEM results, the particles could suffer to a drastic size change, replicating the particle size reduction. The increase of band gap energy can be assessed by bulk defects, indicating delocalization of molecular orbitals in the conduction band. Also, it forms the deep traps in electronic energy. Hence, band edge shift to longer wavelength mimics red-shift of the absorption spectrum [58]. Cr may produce disorder in the host lattice such as micro-strain, point defects, angle distortion which provokes the localized density of states to the absorption, responsible for the variation of band edges [59]. In other hands, the band edge at visible region corresponds to blue-shift. Here, the band edge is shifted to lower wavelength and it is sequential. The prepared material may consist of nanoparticles of different size. Blue shift has speculated from bandgap decrease. Also, 20 nm nanoparticles are spotted, causing blue-shift [60]. Owing to the Cr doping, the Fermi energy levels over the heterojunctions may change to altering bandgap energy. From Tauc plot, the involvement of two bandgap energies implies the degeneracy of the valence band, suggesting effective charge transfer process. The first red-shift type bandgap energy is owing to the internal oxidation-reduction to unit cell of Co_3O_4 i.e from Co^{3+} to Co^{2+} and second blue-shift type bandgap energy is due to the inter-band transitions i.e. from O^{2-} to Co^{2+} which can be considered as absolute bandgap energy [61]. Fig. 7 rolls out the photoluminescence spectrum of undoped Co_3O_4 and Cr-doped Co_3O_4 nanoparticles. In this respect, the undoped Co_3O_4 nanoparticles endow multiple emissions. Although, the deep level emission peak at 460 nm corresponds to the defects. In this case, the sharp peak at 284 nm and strong peak 339–392 nm represents the UV region whereas the rest of the peaks are associated to visible region. Collective emission in UV and visible region of the undoped Co_3O_4 nanoparticles confirmed good crystallinity[62]. The Cr-doped Co_3O_4 nanoparticles emission is akin to the undoped Co_3O_4 nano- particles but peak is shifted to longer wavelengths. Also, the intensity of the photoluminescence spectrum increases. Such high intensity delivery implies the possibility of electron-hole recombination[63]. The observed red-shift is assigned to the defects[64]. Besides, the high intensity indicates the high density of impurity-defect[65]. Further substitution of chromium to cobalt lattice, the intensity of peaks is reduced. Due to that, the photogenerated electron-hole recombination can be suppressed. This specifies the further reduction of nanoparticles size. The effect of chromium to the photoluminescence spectrum can be

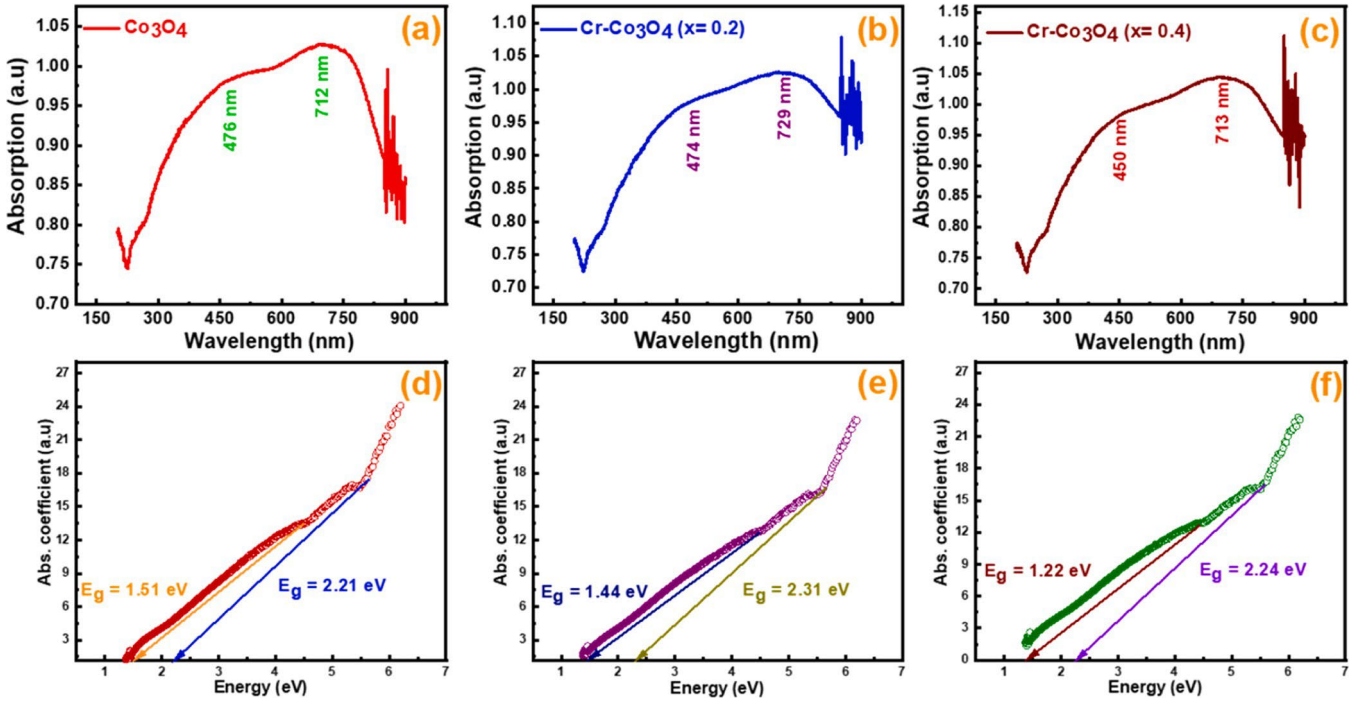

Fig. 6. Optical spectrum of $Cr_xCo_{3-x}O_4$: $x = 0.0, 0.2, 0.4$ nanoparticles: (a-c) absorption, (d-f) bandgap energy.

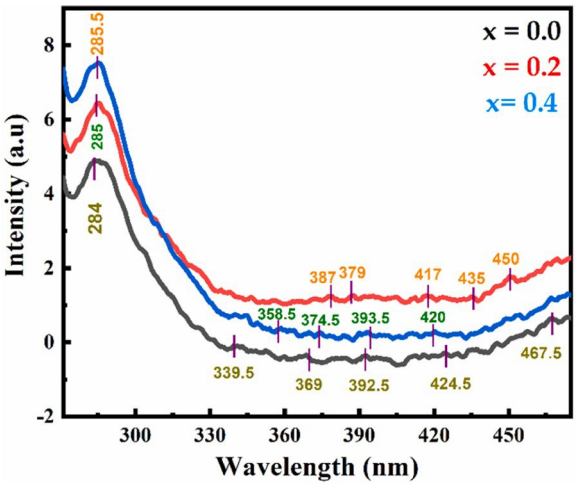

Fig. 7. Photoluminescence spectrum of $Cr_xCo_{3-x}O_4$: x = 0.0, 0.2, 0.4 nanoparticles.

interpreted with the help of XPS analysis. All samples contain only the obvious elements like of cobalt, oxygen and chromium. Therefore, the radiative recombination is not related to the impurities. However, the XPS spectrum demonstrates that the Co_3O_4 and Cr-doped Co_3O_4 nano- particles (x = 0.2)have strong metal-oxygen bond with impurity as chromium oxide which is related to the visible region emission and attributed to the impurity-defects. Here, Cr-doped Co_3O_4 nanoparticles (x = 0.2) have impurity-oxide on the surface because of three peaks are found to be in visible region as compared to undoped nanoparticles. A high concentration of the Cr-doped Co_3O_4 nanoparticles (x = 0.4) had more impurity-oxide owing to the single peak at visible region. Moreover, Co_3O_4 and Cr-doped Co_3O_4 nanoparticles expose the high intense peak around 284–285 nm that facilitates the electron transition from ground to excited state, indicating faster adsorption. The full-width half maximum of the intense peak attributes to the partial crystalline nature of the nanoparticles. The current photoluminescence spectra demonstrate several emission peaks, suggesting approximative outer electronic structure, the capacity of the oxygen atom to join with the cobalt atom is almost the same[66]. On the interface, impurity-defect and electronic defaults are easily created by oxygen atoms. Based on the above discussion, it is clear that impurity-defects have a significant impact on photoluminescence emission.

H_2S gas sensing measurement of undoped and Cr-doped Co_3O_4 sensors is performed by resistance-based method, as shown in Fig. 8(a-c). In all measurements, on increasing temperature, the sensor resistance slumps down. This pertains to the steady conductivity increase of the sensor. Resistance behavior is almost identical for R_a and R_g. In this measurement, the R_a and R_g have maintained the difference in terms of the resistance values, particularly R_a has high value. The R_a unleashes same curvature whereas resistance in the presence of gas unveils similar nature for all sensors[10]. In the presence of gas, the resistance values (R_g) are close to the R_a with difference up to 100 ° C. Apart from this temperature, the resistance maintain large difference as compared to the R_a. These differences occur between 100 and 3 0 0 ° C and thereafter, R_a and R_g could be merge to each other. Due to the temperature increase, more and more free electrons are generated and thereby, the conductivity of the semiconductor sensor increases. Particularly, the generation of free electron can be high during 100 – 300 C and it is saturated on further raise of temperature. Owing to Cr-doping, resistances of R_a and R_g are reduced partly as shown in Fig. 8b. Basically, Cr has shared additional electron and also, generation of free electron is more than the undoped sensor. Free electron may participate the recombination pro- cess by reducing the hole concentration and decreasing the resistance of the sensor material. The dopant influences the bandgap of the material and, it may reduce the distance between the bands which enables a fast movement of the electron. Two third of resistance is decreased due to increasing Cr-doping concentration. This low-resistance suggests the high response of the sensor. According to the measurements, the sensors validate resistance change at ambient temperature. High resistance change is confirmed above ambient temperature. The sensor has ability to operate at room and higher temperatures. The undoped and Cr-doped Co_3O_4 sensor have showed 1.72 and 2.86 responses for 2 ppm H_2S gas

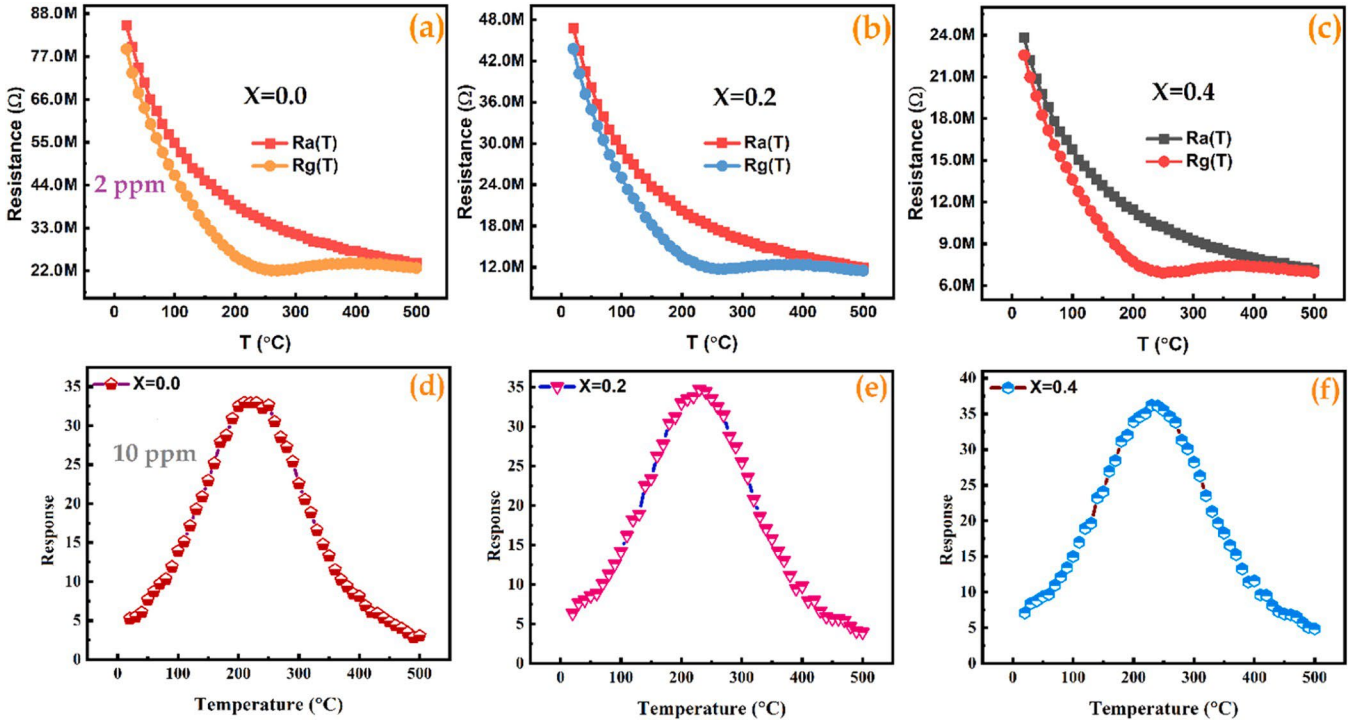

Fig. 8. (a-c) Response to 2 ppm and (d-f) response to 10 ppm under different temperatures $Cr_xCo_{3-x}O_4$: x = 0.0, 0.2, 0.4 sensors.

concentration. This concentration is far below the threshold limit value of H_2S, confirming ultra-low concentration of H_2S gas detection ability. The temperature change rate is 10°C in this measurement which is calibrated the by programmable software (thermocouple-wire)

Sensor operating feasibility has decided from the working temperature. Temperature dispenses the activation energy to the surface of the sensor, in turn, number of electrons released and then reacted to the adsorbed oxygen species [67]. In this work, the wide temperature range of (20 – 500° C) is used to monitor the performance of the sensor at 10 ppm of target gas. Fig. 8(d-f) displays the response variations of undoped and Cr-doped Co_3O_4 sensors at different operating temperatures wherein nearly same nature is identified. According to sensing, response increases and has documented highest response at 230°C and then, due to the increase of temperature, response starts to decrease. The doped sensor has proclaimed the higher response of 7.09 which is higher that of undoped Co_3O_4 sensor at ambient temperature. As from the performance of the sensor, the Cr-doped Co_3O_4 sensor reveals more agile than the undoped Co_3O_4 sensor for detection of the target gas. Mean- time, the undoped Co_3O_4 sensor has showed a competency to sense the gas at ambient and higher temperatures. According to molar ratio, the ratio of $x = 0.4$ doped Co_3O_4 sensor records high response of 36.21. The dopant is also one of the primary causes for increased response. However, the formation of oxygen species is temperature dependent. Furthermore, the reaction rate of target gas at 230°C is greater than the other temperatures, indicating high response. Such higher response is attributed to small size nanostructures of high surface area.

Fig. 9(a-c) manifests the response of undoped and Cr-doped Co_3O_4 sensors to target gas which is varied from 1 ppm to 100 ppm levels (operating temperature (OT)-230°C). Response of individual sensor confirm steady increase owing to increase in H_2S gas concentration. Moreover, all sensors exhibit their potential sensing behavior at low and high concentration detection. According to the results, a sensor with $x = 0.4$ of Cr-doping is the most sensitive. A steep increase of the response is noticed within 1–41 ppm and thereafter, bending-type increase is started. Redox activity can be used to describe the interaction between the H_2S and oxygen species adsorbed on the sensor surface. H_2S is a reducing gas that can played as an electron donor while adsorbed on the surface. Sensor reacts to adsorbed oxygen species by releasing the water and sulfur dioxide owing to the exposure of target gas [68]. More electrons are injected into the conduction band of the sensor material and, electron-hole recombination leads to a sharp increase in the response at certain gas concentration. With increase of gas concentra- tion, the target gas donates greater number of electrons which are used for recombination [9]. However, due to deficient energy, some of the electrons are not able migrate and leaving exposed charges on dopant atom sites that are locked in the crystal lattice which are basically immobile during recombination process. After that, response shows bending-type increase. The doped sensor has adduced to be higher response because dopant has contributed few electrons to the redox activity [69]. As the consequence of this, several electrons are engaged in the adsorption process which eventually increase the response. The cobalt oxide-based sensor reaction is promoted by Cr-doping. Notable decrease in the resistance upon transitioning from air to H_2S environment appears to be beneficial for boosting activity. The interaction of H_2S gas with the sensor surface is believed to be responsible for decrease in the resistance.

Fig. 10 (a-c) shows the response and recovery time of the sensors at 230°C. The response and recovery time values of the undoped sensor are respectively 140 and 200 s. The response time of a sensor is defined as the amount of time takes for its resistance value in air (Ra) to approach 90% of its resistance value in the presence of gas (Rg). Analogously, recovery time is the length of time required after the analyte gas is removed to bring the resistance value in air back to 90%. In contrast, the Cr-doped Co_3O_4 sensor unleash response to target gas within 120 s and recovery time is 190 s. The sensor takes short duration for detection and longer time for recovery. The undoped and doped sensor are taking longer time for response and recovery at room temperature. The response time of the sensor is in the range of 120–140 s and recovery time lies within the 190–200 s. In short, the Cr-doped Co_3O_4 sensor is more dominant than undoped one in dual temperature sensing behavior.

Fig. 11a defines the reproducibility test of the Cr-doped Co_3O_4 sensor at 230°C (30 ppm of target gas). Reproducibility test was carried out for five times. Initially, the response is stayed higher value and then slowed down gradually as per week interval. However, this sensor records the highly low decrease of response in first week. The sensor registers rapid response decrease in second week test. Thereafter, the sensor shows nominal response change to the rest of the test with linear regression. From this observation, the surface of the Cr-doped Co_3O_4 sensor shows itself as an active for adsorption of gas molecules and also, it has never showed a significant decrease of response. After 35 days, sensor exhibits minor change in its their response, indicating long-term stability. Fig. 11b displays the response and recovery time plots of the sensor at same concentration of target gas and working temperature (30 ppm, 230 °C). Before reproducibility test, the response and recovery time values of the sensor are respectively 72 and 88 s. This time consumption is varied in reproducibility test and the difference of the time is 1 s. The time consuming is in good agreement with the response difference which confirms the higher response towards target gas. The Cr-doped Co_3O_4 sensor is exposed to formaldehyde, propane, butane, Xylene and H_2S at room temperature and 30 ppm concentration is used, as shown in Fig. 11c. The sensor has showed responses to all gases but it records the high response to H_2S, implying high selectivity. As compared to other gases, H_2S has more reducing nature which changes the electron density upon its adsorption on the surface for better response[70]. Sensing results of Cr-doped Co_3O_4 sensors are compared to the recently reported work, as shown in Table 1.

According to the survey, the Cr-doped Co_3O_4 sensor material is more versatile than the other materials in terms of surface morphology,

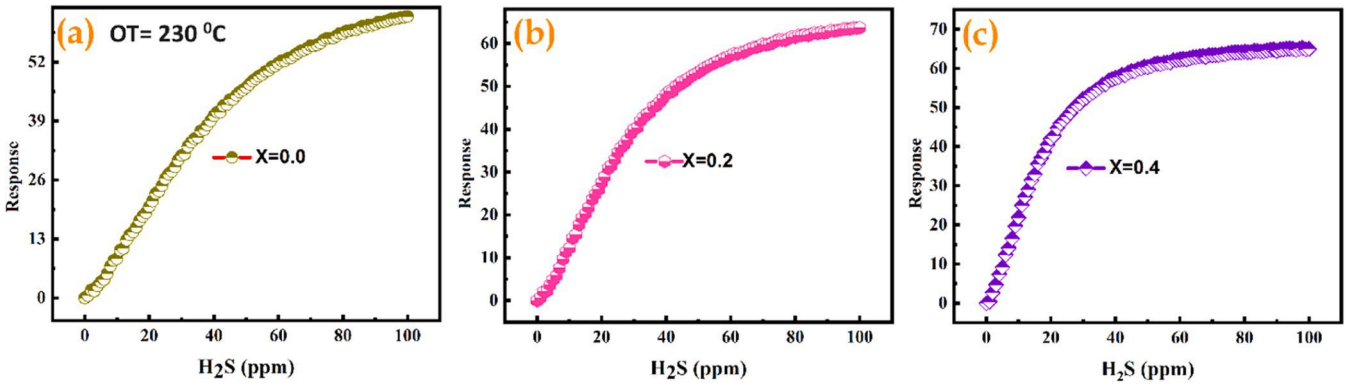

Fig. 9. (a-c) Response of $Cr_xCo_{3-x}O_4$: $x = 0.0, 0.2, 0.4$ sensor under different ppm of gas.

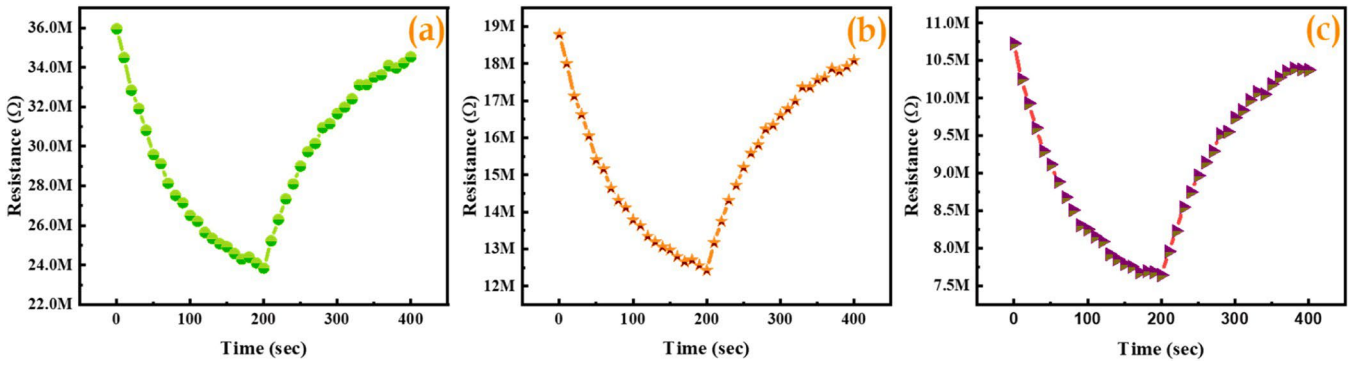

Fig. 10. (a-c) Response/recovery time of $Cr_xCo_{3-x}O_4$: $x = 0.0, 0.2, 0.4$ sensor sensors to 1 ppm gas.

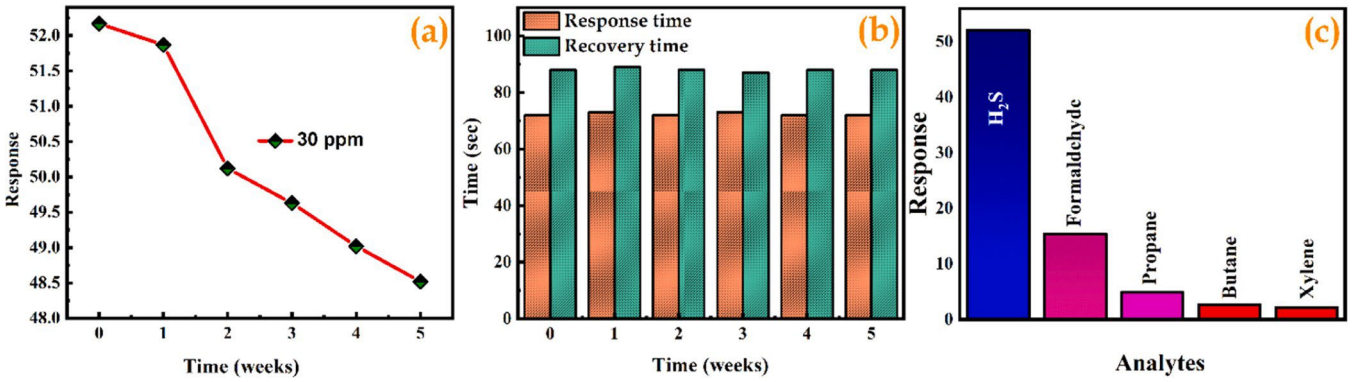

Fig. 11. Response of Cr-doped Co_3O_4 sensor (x=0.4): (a) ageing test, (b) res/recovery time, (c) selectivity.

Table 1
Literature survey approving comparative of H_2S sensor performance of Cr-doped Co_3O_4 sensor with previously reported H_2S sensors.

Material	OT (C)	H_2S gas (ppm)	Res./rec. time (s)	Sensor response	Ref
ZnO	250	10	12/324	0.44	[12]
AuPt-ZnO	300	20	17/151	17.7	[71]
Pt/SnO_2-ZnO	375	05	67/115	30.43	[72]
α-Fe_2O_3/ SnO_2	250	10	13/104	4.3	[73]
Nb_2O_5/SnO_2	275	20	20/97	4.0	[74]
$CuFe_2O_4$	350	10	284/986	4.4	[75]
Rh-doped SnO_2	350	10	06/-	43.8	[76]
BiO	250	10	255/249	0.22	[77]
$BiFeO_3$	350	50	-/-	4.0	[78]
Cu-doped In_2O_3	250	50	24/-	350	[79]
WO_3	275	50	12/20	14.7	[80]
Nb_2O_5@ZnO	400	20	81/69	6.10	[81]
Co_3O_4/ZnO	275	10	76/104	5.0	[82]
CuO/InO_2O_3	70	05	10/3600	229	[83]
WO_3/ CuO	80	05	42/3500	105	[84]
SnO_2/ZnO	75	05	1000/500	10	[85]
Cr- Co_3O_4	**230**	**01**	**120/190**	**01.42**	**This work**

operating temperature, response to extremely low-ppm gas, and potent life-span of active sites. Such facets make them a better contender material for H_2S gas detection. Particularly, we point out that the particle size fall is one of the factors for garnished sensing reaction in the work. Some of the report showed lower operating but their response/recovery time are high. In our case, time consuming is relatively quite low.

Further subjected to response, the reported work unveiled single system response. Our material has two-component system, together, it enhances the h and hig response low

Fig. 12 (a-b) shows the anti-humidity test of the Cr-doped Co_3O_4 sensor at 230° C. The test is carried out on three different relative humidity and 5 ppm of gas is used. The response of the sensor demonstrated decreasing trend with respect to humidity. At 35% RH, the sensor produces the response of 12.95. Thereafter, the sensor showed the response of 8.32 and 5.77–40–45% RH. A little amount of water molecules is adsorbed on the surface due to the hydrogen double bonding which forms thin adsorption layer[86]. Despite, the discontinues adsorption layer hinders the spread of water molecules which favours the best sensing. Further increase of RH, the saltation has formed and also water molecules cover the entire surface of the sensor that restrict the sensor response. Meanwhile, hydronium ions may be produced owing to the high-water molecules. Thus, sensor response falls in high humidity environment. Under the humidity influence, the sensor shows response which implies certain capability to resist the moisture.

In this work, undoped Co_3O_4 sensor is a p-type semiconductor. When a Co_3O_4 sensor bares the surface to dry air, oxygen molecules adsorb on it and can be ionized to create adsorbed oxygen species as shown in Eqs. 1 - 4. Also, the hole accumulation on the Co_3O_4 surface can be caused by the trapped electrons (R_a). As the presence of target gas, the gas molecules are reacted with adsorbed oxygen species that liberate the electrons as illustrated in Eqs. 5 - 7[87–91]. Recombining these released electrons with holes, a hole concentration is decreased with resistance [8].

$$O_{2(gas)} \rightarrow O_{2(ads)} \quad (1)$$

$$O_{2(ads)} + e^- \rightarrow O^-_{2(ads)} \quad (2)$$

$$O^-_{2(ads)} + e^- \rightarrow 2O^-_{(ads)} \quad (3)$$

detection.

$$O^-_{(ads)} + e^- \rightarrow O^-_{2(ads)} \quad (4)$$

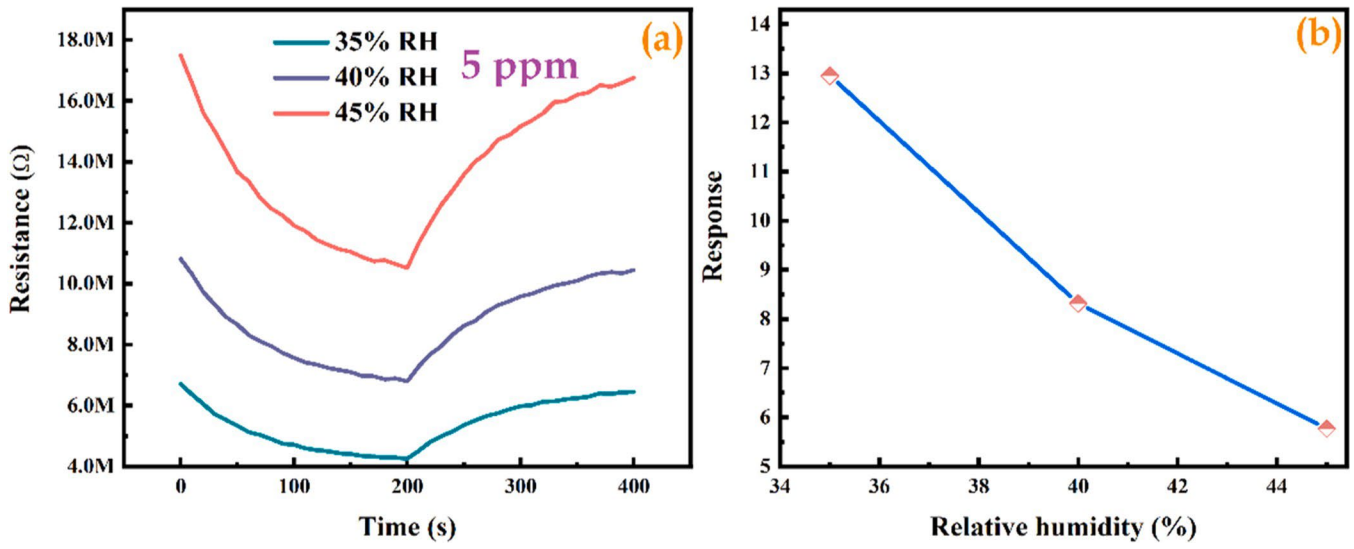

Fig. 12. (a) Anti-humidity test and (b) response of Cr-doped Co_3O_4 sensor (X=0.4).

$$Co_3O_4 + H_2S + O_2 \rightarrow 3CoO + SO_2 + H_2O \quad (5)$$

$$CoO + H_2S \rightarrow CoS + H_2O \quad (6)$$

$$CoS + 3/2O_2 \rightarrow CoO + SO_2 \quad (7)$$

Metallic CoS is formed due to the reaction between H_2S and sensor surface by the following equ 5. The contact between Cr_2O_3 and Co_3O_4 are decreased the resistance of the sensor during the presence of gas. The operating temperature of the sensor exceeds 2 0 0 °C, the CoO has changed into CoS surface[92,93]. The metallic CoS has rich-electrical conductivity and it features the n-type character which leads to dramatically higher electron flow to the sensor. Therefore, the conductivity of sensor has to be scaled up effectively which decreases the resistance of the sensor vastly. The metallic CoS has transformed to CoO through reduction reaction while the sensor placed in air according to equ 5 [94]. The dopant causes the secondary phase formation on the material which is detected by XPS. The Cr_2O_3 and Co_3O_4 made contact and confirms the charge transfer from Co_3O_4 to Cr_2O_3 and holes flee to opposite direction until Fermi level of two system reaches to saturated state. Together two carriers form electron-depletion and hole-accumulation layer, leading to the strong response variation in the sensor. Also, the contact of two-oxide system has actively involved to adsorb the oxygen than single metal oxide. It helps to enhance response of the sensor. Doping has improved the sensor response which is attributed to the electronic. Schematic of sensing mechainsm is depicted in Fig. 13.

sensitization, as chromium has a high specific conductivity. Further, the R_a and R_g values are decreased by Cr-doping which implies conductivity increase. According to electronic sensitization, the exposure of target gas to Cr-doped cobalt oxide sensor surface can cause additional electron release which is lowering the concentration of hole and thereby, the resistance R_g is decreased[95]. With increase of dopant concentration, R_g is further decreased. Additionally, the doping effect reduces the particle size which may provide higher effective surface area for adsorption. As a result, the sensor responds to the target gas more effectively.

4. Conclusion

The Cr-doped cobalt oxide spherical nanoparticles are prepared through simple cost-effective chemical precipitation method. Owing to the Cr-doping, the chromium oxide and doped-cobalt oxide system are facilitated which provides greater number of adsorption sites and made easy path for effective sensing reaction on the sensor. The defect of

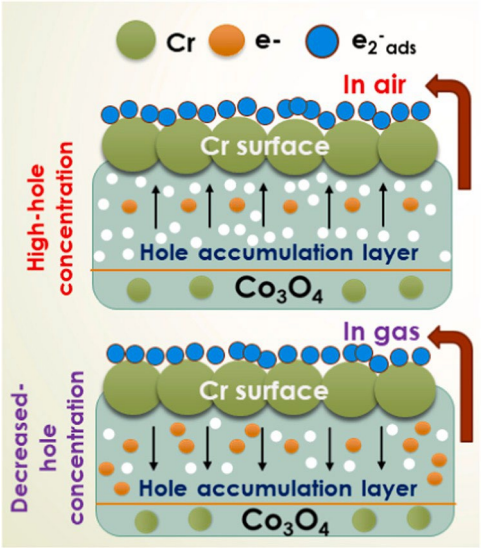

Fig. 13. Schematic of gas sensing mechanism of Cr-doped Co3O4 sensor.

chromium oxide is further helps to increase the conductivity of doped sensor that augments their sensing capacity. The emerge of double- metal oxide emphasizes the better sensing than the single-metal oxide system in this work. The sensor revealed imminent response to 1 ppm around 120 s and 200 s for recovery time. This time scale is subjected to future research in this material. The sensor showed high reproducibility which pledges the long-term stability. The Cr-doped sensor records three-fold response increase (36.21) to 10 ppm and nearly ~3 response to 2 ppm, implying that these sensors are excellent options for H_2S sensing applications.

CRediT authorship contribution statement

Manickam Selvaraj: Resources. **Iulian Petrila:** Supervision. **Rajaram S. Mane:** Validation. **Craig E. Banks:** Conceptualization. **Robert D. Crapnell:** Methodology. **G. Ayyannan:** Visualization. **Manikandan Venkatraman:** Writing – original draft.

Declaration of Competing Interest

The authors declare that they have no known competing financial interests or personal relationships that could have appeared to influence the work reported in this paper.

Data availability

The data that has been used is confidential.

Acknowledgements

The authors extend their appreciation to the Deanship of Scientific Research at King Khalid University for funding this work through the large group project under grant number (132/45).

Appendix A. Supporting information

Supplementary data associated with this article can be found in the online version at doi:10.1016/j.jece.2024.112697.

References

[1] Z. Li, Y. Huang, S. Zhang, W. Chen, Z. Kuang, D. Ao, W. Liu, Y. Fu, A fast response & recovery H_2S gas sensor based on α-Fe2O3 nanoparticles with ppb level detection limit, J. Hazard Mater. 300 (2015) 167–174.

[2] S.K. Pandey, K.H. Kim, K.T. Tang, A review of sensor-based methods for monitoring hydrogen sulfide, TrAC Trends Anal. Chem. 32 (2012) 87–99.

[3] J. Wang, Y. Ren, H. Liu, Z. Li, X. Liu, Y. Deng, X. Fang, Ultrathin 2D $NbWO_6$ perovskite semiconductor based gas sensors with ultrahigh selectivity under low working temperature, Adv. Mater. 34 (2022) 2104958.

[4] Y. Li, W. Luo, N. Qin, J. Dong, J. Wei, W. Li, S. Feng, J. Chen, J. Xu, A.A. Elzatahry, M.H. Es-Saheb, Y. Deng, D. Zhao, Supporting Information Highly Ordered Mesoporous Tungsten Oxides with a Large Pore Size and Crystalline Framework for H2S Sensing, 126 (2014) 9181-9186.

[5] G. Huang, E. He, Z. Wang, H. Fan, J. Shangguan, E. Croiset, Z. Chen, Synthesis and characterization of γ-Fe_2O_3 for H_2S removal at low temperature, Ind. Eng. Chem. Res 54 (2015) 8469–8478.

[6] C. Liu, R. Zhang, S. Wei, J. Wang, Y. Liu, M. Li, R. Liu, Selective removal of H2S from biogas using a regenerable hybrid TiO_2/zeolite composite, Fuel 157 (2015) 183–190.

[7] N. Luo, M. Guo, H. Cai, X. Li, X. Wang, Z. Cheng, Z. Xue, J. Xu, Engineering a heterophase interface by tailoring the Pt coverage density on an amorphous Ru surface for ultrasensitive H_2S detection, ACS Sens 8 (2023) 2237–2246.

[8] M.S. Wagh, L.A. Patil, T. Seth, D.P. Amalnerkar, Surface cupricated SnO_2-ZnO thick films as a H_2S gas sensor, Mater. Chem. Phys. 84 (2004) 228–233.

[9] S. Poongodi, P.S. Kumar, D. Mangalaraj, N. Ponpandian, P. Meena, Y. Masuda, C. Lee, Electrodeposition of WO_3 nanostructured thin films for electrochromic and H_2S gas sensor applications, J. Alloy. Compd. 719 (2017) 71–81.

[10] X. Hu, Z. Zhu, C. Chen, T. Wen, X. Zhao, L. Xie, Highly sensitive H_2S gas sensors based on Pd-doped CuO nanoflowers with low operating temperature, Sens Actuators B Chem. 253 (2017) 809–817.

[11] M.A. Haija, A.F.S. Abu-Hani, N. Hamdan, S. Stephen, A.I. Ayesh, Characterization of H2S gas sensor based on $CuFe_2O_4$nanoparticles, J. Alloy. Compd. 690 (2017) 461–468.

[12] U.T. Nakate, Y.T. Yu, S. Park, Hydrothermal synthesis of ZnO nanoflakes composed of fine nanoparticles for H_2S gas sensing application, Ceram. Int 48 (2022) 28822–28829.

[13] S. Hussain, J.N. Okai Amu-Darko, M. Wang, A.A. Alothman, M. Ouladsmane, S. A. Aldossari, M.S. Khan, G. Qiao, G. Liu, CuO-decorated MOF derived ZnO polyhedral nanostructures for exceptional H_2S gas detection, Chemosphere 317 (2023) 137827.

[14] T. Shi, H. Hou, S. Hussain, C. Ge, M.A. Alsaiari, A.S. Alkorbi, G. Liu, R. Alsaiari, G. Qiao, Efficient detection of hazardous H_2S gas using multifaceted Co_3O_4/ZnO hollow nanostructures, Chemosphere 287 (2022) 132178.

[15] J.N. Okai Amu-Darko, S. Hussain, X. Zhang, A.A. Alothman, M. Ouladsmane, M. T. Nazir, G. Qiao, G. Liu, Metal-organic frameworks-derived In_2O_3/ZnO porous hollow nanocages for highly sensitive H_2S gas sensor, Chemosphere 314 (2023) 137670.

[16] S. Iravani, R.S. Varma, Sustainable synthesis of cobalt and cobalt oxide nanoparticles and their catalytic and biomedical applications, Green. Chem. 22 (2020) 2643–2661.

[17] M. Hassan, S. Liu, Z. Liang, S. Hussain, J. Liu, G. Liu, G. Qiao, Revisiting traditional and modern trends in versatile 2D nanomaterials: Synthetic strategies, structural stability, and gas-sensing fundamentals, J. Adv. Ceram. 12 (2023) 2149–2246.

[18] J.N.O. Amu-Darko, S. Hussain, Q. Gong, X. Zhang, Z. Xu, M. Wang, G. Liu, G. Qiao, Highly sensitive In_2O_3/PANI nanosheets gas sensor for NO_2 detection, J. Environ. Chem. Eng. 11 (2023) 109211.

[19] J. Tan, S. Hussain, C. Ge, M. Wang, S. Shah, G. Liu, G. Qiao, ZIF-67 MOF-derived unique double-shelled Co_3O_4/$NiCo_2O_4$ nanocages for superior Gas-sensing performances, Sens Actuators B Chem. 303 (2020) 127251.

[20] M. Martin, U. Koops, N. Lakshmi, Reactivity of solids studied by in situ XAS and XRD, Solid State Ion.-. 172 (2004) 357–363.

[21] G. Jacobs, Y. Ji, B.H. Davis, D. Cronauer, A.J. Kropf, C.L. Marshall, Fischer-Tropsch synthesis: temperature programmed EXAFS/XANES investigation of the influence of support type, cobalt loading, and noble metal promoter addition to the reduction behavior of cobalt oxide particles, Appl. Catal. A Gen. 333 (2007) 177–191.

[22] V. Papaefthimiou, T. Dintzer, V. Dupuis, A. Tamion, F. Tournus, D. Teschner, M. Ha¨vecker, A. Knop-Gericke, R. Schlo¨gl, S. Zafeiratos, When a metastable oxide stabilizes at the nanoscale: wurtzite CoO formation upon dealloying of PtCo nanoparticles, J. Phys. Chem. Lett. 2 (2011) 900–904.

[23] M. Staniuk, O. Hirsch, N. Kra¨nzlin, R. Bo¨hlen, W. Van Beek, P.M. Abdala, D. Koziej, Puzzling mechanism behind a simple synthesis of cobalt and cobalt oxide nanoparticles: in situ synchrotron X-ray absorption and diffraction studies, Chem. Mater. 26 (2014) 2086–2094.

[24] J. Lee, B. Jeong, J.D. Ocon, Oxygen electrocatalysis in chemical energy conversion and storage technologies, Curr. Appl. Phys. 13 (2013) 309–321.

[25] C.R. Raj, A. Samanta, S.H. Noh, S. Mondal, T. Okajima, T. Ohsaka, Emerging new generation electrocatalysts for the oxygen reduction reaction, J. Mater. Chem. A Mater. 4 (2016) 11156–11178.

[26] B. Paul, P. Bhanja, S. Sharma, Y. Yamauchi, Z.A. Alothman, Z.L. Wang, R. Bal, A. Bhaumik, Morphologically controlled cobalt oxide nanoparticles for efficient oxygen evolution reaction, J. Colloid Interface Sci. 582 (2021) 322–332.

[27] S. Guan, J. Zhou, S. Sun, Q. Peng, X. Guo, B. Liu, X. Zhou, Y. Tang, Nonmetallic Se/N Co-doped amorphous carbon anode collaborates to realize ultra-high capacity and fast potassium storage for potassium dual-ion batteries, Adv. Funct. Mater. (2024) 2314890.

[28] D. Xie, M. Zhang, Q. Liu, Y. Lin, A. Yu, Y. Tang, Organic-inorganic conformal extending high-purity metal nanosheets for robust electrochemical lithium-ion storage, Adv. Funct. Mater. 33 (2023) 2306291.

[29] R. Yang, W. Yao, L. Zhou, F. Zhang, Y. Zheng, C.S. Lee, Y. Tang, Secondary amines functionalized organocatalytic iodine redox for high-performance aqueous dual-ion batteries, Adv. Mater. 1 (2024) 2314247.

[30] D. M, S. Ch, R.K. E, R. P.N, N.K. Mohan, M. Sher Singh, C.L. Prajapat, A. Verma, D. L. Sastry, Evaluation of structural and dielectric properties of Mn^{2+}-substituted Zn-spinel ferrite nanoparticles for gas sensor applications, Sens Actuators B Chem. 316 (2020) 128127.

[31] E. Ranjith Kumar, P. Siva Prasada Reddy, G. Sarala Devi, S. Sathiyaraj, Structural, dielectric and gas sensing behavior of Mn substituted spinel MFe_2O_4 (M=Zn, Cu, Ni, and Co) ferrite nanoparticles, J. Magn. Magn. Mater. 398 (2016) 281–288.

[32] C. Srinivas, E. Ranjith Kumar, B.V. Tirupanyam, S. Singh Meena, P. Bhatt, C. L. Prajapat, T.V. Chandrasekhar Rao, D.L. Sastry, Study of magnetic behavior in co-precipitated Ni–Zn ferrite nanoparticles and their potential use for gas sensor applications, J. Magn. Magn. Mater. 502 (2020) 166534.

[33] E. Ranjith Kumar, R. Jayaprakash, G. Sarala Devi, P. Siva Prasada Reddy, Synthesis of Mn substituted $CuFe_2O_4$ nanoparticles for liquefied petroleum gas sensor applications, Sens Actuators B Chem. 191 (2014) 186–191.

[34] E.R. Kumar, C. Srinivas, M.S. Seehra, M. Deepty, I. Pradeep, A.S. Kamzin, M.V. K. Mehar, N.K. Mohan, Particle size dependence of the magnetic, dielectric and gas sensing properties of Co substituted $NiFe_2O_4$ nanoparticles, Sens Actuators A Phys. 279 (2018) 10–16.

[35] P. Gibot, L. Vidal, Original synthesis of chromium (III) oxide nanoparticles, J. Eur. Ceram. Soc. 30 (2010) 911–915.

[36] R.P. Singh, R.K. Singh, Theoretical study of temperature dependent acoustic attenuation and non-linearity parameters in alkali metal hydride and deuteride, Mater. Chem. Phys. 124 (2010) 575–579.

[37] S.R. Morrison, selectivity in semiconductor gas sensors, Sens Actuators B Chem. 12 (1987) 425–440.

[38] B.K. Miremadi, R.C. Singh, Z. Chen, S.R. Morrison, K. Colbow, Chromium oxide gas sensors for the detection of oxygen and nitrogen oxide hydrogen, Sens Actuators B Chem. 21 (1994) 1–4.

[39] T.Y. Ma, S. Dai, M. Jaroniec, S.Z. Qiao, Metal-organic framework derived hybrid Co_3O_4-carbon porous nanowire arrays as reversible oxygen evolution electrodes, J. Am. Chem. Soc. 136 (2014) 13925–13931.

[40] F. Ali, N.R. Khalid, Facile synthesis and properties of chromium-doped cobalt oxide (Cr-doped Co_3O_4) nanostructures for supercapacitor applications, Appl. Nanosci. 10 (2020) 1481–1488.

[41] R.S. Reena, A. Aslinjensipriya, M. Jose, S.J. Das, Investigation on structural, optical and electrical nature of pure and Cr-incorporated cobalt oxide nanoparticles prepared via co-precipitation method for photocatalytic activity of methylene blue dye, J. Mater. Sci. Mater. Electron. 31 (2020) 22057–22074.

[42] T. Baidya, T. Murayama, P. Bera, O.V. Safonova, P. Steiger, N.K. Katiyar, K. Biswas, M. Haruta, Low-temperature CO oxidation over combustion made Fe- and Cr-doped Co_3O_4 catalysts: role of dopant's nature toward achieving superior catalytic activity and stability, J. Phys. Chem. C. 121 (2017) 15256–15265.

[43] J. Mao, K. Dai, M. Xuan, G. Shao, R. Qiao, W. Yang, V.S. Battaglia, G. Liu, Effect of chromium and niobium doping on the morphology and electrochemical performance of high-voltage spinel $LiNi_{0.5}Mn_{1.5}O_4$ cathode material, ACS Appl. Mater. Interfaces 8 (2016) 9116–9124.

[44] Y. Zhang, M. Zhu, S. Xu, H. Zhou, H. Qi, H. Wang, Zeolitic imidazolate framework derived cobalt oxide anchored bacterial cellulose: a good template with improved H_2O adsorption ability and its enhanced hydrogen evolution performance, Electro Acta 353 (2020) 136499.

[45] N.H. Shalaby, Photocatalytic performance of organically templated Cr-doped Co_3O_4 in remediation of industrial wastewater: effect of order–disorder in the lattice, Arab J. Sci. Eng. 48 (2023) 7425–7436.

[46] D.V. Sivkov, O.V. Petrova, S.V. Nekipelov, A.S. Vinogradov, R.N. Skandakov, K. A. Bakina, S.I. Isaenko, A.M. Ob'edkov, B.S. Kaverin, I.V. Vilkov, V.N. Sivkov, Quantitative characterization of oxygen-containing groups on the surface of carbon materials: XPS and NEXAFS study, Appl. Sci. 12 (2022) 7744.

[47] S. Malkhandi, P. Trinh, A.K. Manohar, A. Manivannan, M. Balasubramanian, G.K. S. Prakash, S.R. Narayanan, Design insights for tuning the electrocatalytic activity of perovskite oxides for the oxygen evolution reaction, J. Phys. Chem. C. 119 (2015) 8004–8013.

[48] S.N. Falaein Moridon, M.N. Ikhmal Salehmin, K. Arifin, L.J. Minggu, M.B. Kassim, Synthesis of cobalt oxide on fto by hydrothermal method for photoelectrochemicalwater splitting application, Appl. Sci. (Switz.) 11 (2021) 3031.

[49] R. Kalia, A. Chauhan, R. Verma, M. Sharma, K.M. Batoo, R. Kumar, S. Hussain, S. Ghotekar, M.F. Ijaz, Photocatalytic degradation properties of Li-Cr ions substituted $CoFe_2O_4$ nanoparticles for wastewater treatment application, Phys. Status Solidi (A) Appl. Mater. Sci. 219 (2022) 2100539.

[50] M.C. Biesinger, C. Brown, J.R. Mycroft, R.D. Davidson, N.S. McIntyre, X-ray photoelectron spectroscopy studies of chromium compounds, Surf. Interface Anal. 36 (2004) 1550–1563.

[51] G.E. Collins, N.R. Armstrong, J.W. Pankow, C. Oden, R. Brina, C. Arbour, J. -P. Dodelet, Thin film sensors: the role of defects and impurity sites in controlling sensor response and selectivity, J. Vac. Sci. Technol. A: Vac., Surf., Films 11 (1993) 1383–1391.

[52] J. Singh, V. Verma, R. Kumar, Preparation and structural, optical studies of Al substituted chromium oxide (Cr_2O_3) nanoparticles, Vacuum 159 (2019) 282–286.

[53] C. Ravi Dhas, R. Venkatesh, K. Jothivenkatachalam, A. Nithya, B. Suji Benjamin, A. Moses Ezhil Raj, K. Jeyadheepan, C. Sanjeeviraja, Visible light driven photocatalytic degradation of Rhodamine B and Direct Red using cobalt oxide nanoparticles, Ceram. Int 41 (2015) 9301–9313.

[54] B. De Rivas, R. Lo´pez-Fonseca, C. Jim´enez-Gonz´alez, J.I. Guti´errez-Ortiz, Synthesis, characterisation and catalytic performance of nanocrystalline Co_3O_4 for gas-phase chlorinated VOC abatement, J. Catal. 281 (2011) 88–97.

[55] K. Thangavelu, K. Parameswari, K. Kuppusamy, Y. Haldorai, A simple and facile method to synthesize Co_3O_4 nanoparticles from metal benzoate dihydrazinate complex as a precursor, Mater. Lett. 65 (2011) 1482–1484.

[56] F. Gu, C. Li, Y. Hu, L. Zhang, Synthesis and optical characterization of Co_3O_4 nanocrystals, J. Cryst. Growth 304 (2007) 369–373.

[57] W. Shi, N. Chopra, Surfactant-free synthesis of novel copper oxide (CuO) nanowire - cobalt oxide (Co_3O_4) nanoparticle heterostructures and their morphological control, J. Nanopart. Res. 13 (2011) 851–868.

[58] M. Ghiasi, A. Malekzadeh, H. Mardani, Synthesis and optical properties of cubic Co3O4 nanoparticles via thermal treatment of a trinuclear cobalt complex, Mater. Sci. Semicond. Process 42 (2016) 311–318.

[59] A.N. Naveen, S. Selladurai, Tailoring structural, optical and magnetic properties of spinel type cobalt oxide (Co_3O_4) by manganese doping, Phys. B Condens Matter 457 (2015) 251–262.

[60] S. Thota, A. Kumar, J. Kumar, Optical, electrical and magnetic properties of Co_3O_4 nanocrystallites obtained by thermal decomposition of sol-gel derived oxalates, Mater. Sci. Eng. B Solid State Mater. Adv. Technol. 164 (2009) 30–37.

[61] T. Merciris, F. Valensi, A. Hamdan, Synthesis of nickel and cobalt oxide nanoparticles by pulsed underwater spark discharges, J. Appl. Phys. 129 (2021) 063303.

[62] M.F. Valan, A. Manikandan, S.A. Antony, A novel synthesis and characterization studies of magnetic Co_3O_4 nanoparticles, J. Nanosci. Nanotechnol. 15 (2015) 4580–4586.

[63] S. Thambidurai, P. Gowthaman, M. Venkatachalam, S. Suresh, M. Kandasamy, Morphology dependent photovoltaic performance of zinc oxide-cobalt oxide nanoparticle/nanorod composites synthesized by simple chemical co-precipitation method, J. Alloy. Compd. 852 (2021) 156997.

[64] M.A. Ahmed, S.T. Bishay, M.M. El-Masry, Structural and topographic study of ceria nanoparticles prepared via different techniques, Superlattices Micro 77 (2015) 240–255.

[65] X. Zhang, F. Hou, H. Li, Y. Yang, Y. Wang, N. Liu, Y. Yang, A strawsheave-like metal organic framework Ce-BTC derivative containing high specific surface area for improving the catalytic activity of CO oxidation reaction, Microporous Mesoporous Mater. 259 (2018) 211–219.

[66] P. Prameela, J.R. Ramya, J. Gajendiran, S. Gnanam, K. Ramachandran, S.G. Raj, G. R. Kumar, Structural, magnetic, and antibacterial activity of the pure, Zn-doped, and Zn-doped/sugar-assisted coprecipitation synthesized semicrystalline Co_3O_4 compound, J. Mol. Struct. 1292 (2023) 136154.

[67] X. Wang, S. Li, L. Xie, X. Li, D. Lin, Z. Zhu, Low-temperature and highly sensitivity H_2S gas sensor based on ZnO/CuO composite derived from bimetal metal-organic frameworks, Ceram. Int 46 (2020) 15858–15866.

[68] V.V. Malyshev, A.V. Pislyakov, SnO_2-based thick-film-resistive sensor for H_2S detection in the concentration range of 1–10 mg m^{-3}, Sens Actuators B Chem. 47 (1998) 181–188.

[69] D. Li, Y. Tang, D. Ao, X. Xiang, S. Wang, X. Zu, Ultra-highly sensitive and selective H_2S gas sensor based on CuO with sub-ppb detection limit, Int J. Hydrog. Energy 44 (2019) 3985–3992.

[70] E. Afjeh-Dana, E. Asadian, M.R. Razzaghi, H. Rafii-Tabar, P. Sasanpour, Deflection-based laser sensing platform for selective and sensitive detection of H_2S using plasmonic nanostructures, Sci. Rep. 12 (2022) 15789.

[71] Y. Liu, L.Y. Zhu, P. Feng, C. Dang, M. Li, H.L. Lu, L. Gao, Bimetallic AuPt alloy nanoparticles decorated on ZnO nanowires towards efficient and selective H_2S gas sensing, Sens Actuators B Chem. 367 (2022) 132024.

[72] X.Y. Wu, L.Y. Zhu, J. Sun, K.Y. Zhu, X.Y. Miao, M.Y. Liu, X.F. Zhao, H.L. Lu, Pt Nanoparticle-modified SnO_2-ZnO core-shell nanosheets on microelectromechanical systems for enhanced H_2S detection, ACS Appl. Nano Mater. 5 (2022) 6627–6636.

[73] X.Y. Miao, L.Y. Zhu, X.Y. Wu, L.W. Mao, X.H. Jin, H.L. Lu, Precise preparation of α-Fe_2O_3/SnO_2 core-shell nanowires via atomic layer deposition for selective MEMS-based H_2S gas sensor, Sens Actuators B Chem. 378 (2023) 133111.

[74] L.W. Mao, L.Y. Zhu, T. Tao Wu, L. Xu, X.H. Jin, H.L. Lu, Excellent long-term stable H_2S gas sensor based on Nb_2O_5/SnO_2 core-shell heterostructure nanorods, Appl. Surf. Sci. 602 (2022) 154339.

[75] P.H. Phuoc, N. Van Hoang, N.M. Hung, P.T. Hung, P.D. Hoat, N. Van Hieu, On-chip $CuFe_2O_4$ nanofiber for conductometric NO_2 and H_2S gas-sensors, Sens Actuators B Chem. 380 (2023) 133306.

[76] K. Inyawilert, M. Punginsang, A. Wisitsoraat, A. Tuantranont, C. Liewhiran, Graphene/Rh-doped SnO_2 nanocomposites synthesized by electrochemical exfoliation and flame spray pyrolysis for H_2S sensing, J. Alloy. Compd. 916 (2022) 165431.

[77] K.D. Bhalerao, Y.T. Nakate, S.P. Choudhury, U.T. Nakate, M.A. Yewale, S. L. Kadam, R.S. Ingole, S.C. Kulkarni, Y.B. Khollam, Synthesis, characterizations, and hydrogen sulfide gas sensing application of BiO_x (x = 1, 1.5) nanostructures, Int J. Hydrog. Energy 48 (2023) 840–848.

[78] T. Bagwaiya, S. Bhattacharya, V. Shelke, S. Samanta, M. Kaur, A.K. Debnath, Enhanced H_2S gas sensing performance of Ca-doped Bismuth Ferrite thick films, Mater. Sci. Semicond. Process 148 (2022) 106782.

[79] Y. Zhang, S. Han, M. Wang, S. Liu, G. Liu, X. Meng, Z. Xu, M. Wang, G. Qiao, Electrospun Cu-doped In_2O_3 hollow nanofibers with enhanced H_2S gas sensing performance, J. Adv. Ceram. 11 (2022) 427–442.

[80] X. Wang, J. Lu, W. Han, P. Cheng, Y. Wang, J. Sun, J. Ma, P. Sun, H. Zhang, Y. Sun, G. Lu, Carbon modification endows WO_3 with anti-humidity property and long-term stability for ultrafast H_2S detection, Sens Actuators B Chem. 350 (2022) 130884.

[81] T.T. Wu, L.Y. Zhu, X.Y. Wu, X.Y. Miao, L.W. Mao, X.H. Jin, H.L. Lu, Hierarchical Nb_2O_5@ZnO hetero-branched nanorods for enhanced H2S gas sensing, Sens Actuators B Chem. 374 (2023) 132806.

[82] T. Shi, H. Hou, S. Hussain, C. Ge, M.A. Alsaiari, A.S. Alkorbi, G. Liu, R. Alsaiari, G. Qiao, Efficient detection of hazardous H_2S gas using multifaceted Co_3O_4/ZnO hollow nanostructures, Chemosphere 287 (2022) 132178.

[83] S. Li, L. Xie, M. He, X. Hu, G. Luo, C. Chen, Z. Zhu, Metal-organic frameworks-derived bamboo-like CuO/In_2O_3 Heterostructure for high-performance H_2S gas sensor with Low operating temperature, Sens Actuators B Chem. 310 (2020) 127828.

[84] M. He, L. Xie, X. Zhao, X. Hu, S. Li, Z.G. Zhu, Highly sensitive and selective H2S gas sensors based on flower-like WO_3/CuO composites operating at low/room temperature, J. Alloy. Compd. 788 (2019) 36–43.

[85] J. Chang, Z. Deng, X. Fang, C. Hu, L. Shi, T. Dai, M. Li, S. Wang, G. Meng, Heterostructural $(Sr_{0.6}Bi_{0.3}0_5)_2Bi_2O_7$/ZnO for novel high-performance H2S sensor operating at low temperature, J. Hazard Mater. 414 (2021) 125500.

[86] H. Sheng, S. Ma, T. Han, P. Yun, T. Yang, J. Ren, A highly sensitivity and anti-humidity gas sensor for ethanol detection with $NdFeO_3$ nano-coral granules, Vacuum 195 (2022) 110642.

[87] R.V. Poonguzhali, E. Ranjith Kumar, T. Pushpagiri, A. Steephen, N. Arunadevi, S. Baskoutas, Lemon juice (natural fuel) assisted synthesis of MgO nanorods for LPG gas sensor applications, Solid State Commun. 325 (2021) 114161.

[88] R. Vandamar Poonguzhali, E. Ranjith Kumar, N. Arunadevi, C. Srinivas, M. E. Khalifa, S. Abu-Melha, N.M. El-Metwaly, Natural citric acid assisted synthesis of CuO nanoparticles: evaluation of structural, optical, morphological properties and colloidal stability for gas sensor applications, Ceram. Int 48 (2022) 26287–26293.

[89] R.V. Poonguzhali, E.R. Kumar, C. Srinivas, M. Alshareef, M.M. Aljohani, A. A. Keshk, N.M. El-Metwaly, N. Arunadevi, Natural lemon extract assisted green synthesis of spinel Co_3O_4 nanoparticles for LPG gas sensor application, Sens Actuators B Chem. 377 (2023) 133036.

[90] T. Pushpagiri, E. Ranjith Kumar, A. Ramalingam, A.F. Abd El-Rehim, C. Srinivas, Effect of doping concentration on structural, vibrational, morphological and colloidal stability of Zn doped NiO nanoparticles for gas sensor applications, Ceram. Int 49 (2023) 23903–23911.

[91] S. Ananthi, M. Kavitha, A. Balamurugan, E. Ranjith Kumar, G. Magesh, A.F. Abd El-Rehim, C. Srinivas, P. Anilkumar, J. Suryakanth, C. Sharmila Rahale, Synthesis, analysis and characterization of Camellia sinensis mediated synthesis of NiO nanoparticles for ethanol gas sensor applications, Sens Actuators B Chem. 387 (2023) 133742.

[92] J.N.O. Amu-Darko, S. Hussain, E. Issaka, M. Wang, A.A. Alothman, S. Lei, G. Qiao, G. Liu, Nanosheet assembled NiO-doped-ZnO flower-like sensors for highly sensitive hydrogen sulfide gas detection, Ceram. Int 1 (2024) 1–10.

[93] J.N.O. Amu-Darko, S. Hussain, X. Zhang, M. Ouladsmane, E. Issaka, S. Ali, M. Wang, G. Qiao, Exploring the gas-sensing properties of MOF-derived TiN@CuO as a hydrogen sulfide sensor, Chemosphere 337 (2023) 139401.

[94] S. Hussain, J.N. Okai Amu-Darko, M. Wang, A.A. Alothman, M. Ouladsmane, S. A. Aldossari, M.S. Khan, G. Qiao, G. Liu, CuO-decorated MOF derived ZnO polyhedral nanostructures for exceptional H_2S gas detection, Chemosphere 317 (2023) 137827.

[95] C. Yang, F. Xiao, J. Wang, X. Su, 3D flower- and 2D sheet-like CuO nanostructures: microwave-assisted synthesis and application in gas sensors, Sens Actuators B Chem. 207 (2015) 177–185.